ELSEVIER

Materials Science and Engineering B87 (2001) 204–213

MATERIALS SCIENCE & ENGINEERING B

www.elsevier.com/locate/mseb

Direct energy gap group IV semiconductor alloys and quantum dot arrays in Sn_xGe_{1-x}/Ge and Sn_xSi_{1-x}/Si alloy systems

Regina Ragan, Kyu S. Min [1], Harry A. Atwater *

Thomas J. Watson Laboratory of Applied Physics, California Institute of Technology, MS 128-95, Pasadena, CA 91125, USA

Abstract

The narrow gap semiconductor alloys Sn_xGe_{1-x} and Sn_xSi_{1-x} offer the possibility for engineering tunable direct energy gap Group IV semiconductor materials. For pseudomorphic Sn_xGe_{1-x} alloys grown on Ge (001) by molecular beam epitaxy, an indirect-to-direct bandgap transition with increasing Sn composition is observed, and the effects of misfit on the bandgap analyzed in terms of a deformation potential model. Key results are that pseudomorphic strain has only a very slight effect on the energy gap of Sn_xGe_{1-x} alloys grown on Ge (001) but for Sn_xGe_{1-x} alloys grown on Ge (111) no indirect-to-direct gap transition is expected. In the Sn_xSi_{1-x} system, ultrathin pseudomorphic epitaxially-stabilized α-Sn_xSi_{1-x} alloys are grown on Si (001) substrates by conventional molecular beam epitaxy. Coherently strained α-Sn quantum dots are formed within a defect-free Si (001) crystal by phase separation of the thin Sn_xSi_{1-x} layers embedded in Si (001). Phase separation of the thin alloy film, and subsequent evolution occurs via growth and coarsening of regularly-shaped α-Sn quantum dots that appear as 4–6 nm diameter tetrakaidecahedra with facets oriented along elastically soft ⟨100⟩ directions. Attenuated total reflectance infrared absorption measurements indicate an absorption feature due to the α-Sn quantum dot array with onset at ~ 0.3 eV and absorption strength of 8×10^3 cm^{-1}, which are consistent with direct interband transitions.

Keywords: Energy gap; Semiconductor alloys; Sn quantum dot

1. Introduction

Group IV semiconductor alloys containing Sn, such as Sn_xGe_{1-x} and Sn_xSi_{1-x} hold potential for band-structure engineering of tunable narrow direct gap group IV semiconductors with potential applications in Si-based infrared optoelectronics and thermophotovoltaics. Notably, the Sn_xGe_{1-x} alloy is the only group IV semiconductor known to exhibit a direct energy band gap [1]. The alloy effect on E_g, Γ_7 of homogeneous, relaxed Sn_xGe_{1-x} is found to be $0.35 < E_g < 0.8$ eV for $0.15 < x < 0$ [1]. Tight binding calculations [2] predict the indirect transition to occur at near $x = 0.22$, while experiments indicate the transition occurs near $x = 0.09$. The earlier onset of the indirect to direct energy band gap transition is serendipitous because Sn_xGe_{1-x} is chemically metastable and substitutional Sn incorporation becomes increasingly difficult for $x > 0.20$ [3]. For Sn_xSi_{1-x} alloys, these factors are even more challenging since the Sn composition at which an indirect-to-direct gap transition is expected to occur is much higher. Moreover, the misfit strain is higher, the tendency for Sn surface segregation is more pronounced and the equilibrium solubility of Sn in Si is lower than in Ge. However, temperature-modulated molecular beam epitaxy enables very thin pseudomorphic Sn_xSi_{1-x} layers to be grown on Si substrates. Post-growth annealing results in growth of pseudomorphic α-Sn quantum dots in Si (001) which evolve via phase separation.

2. Sn_xGe_{1-x} film growth and characterization

The Sn_xGe_{1-x} heterostructures described here were grown by molecular beam epitaxy. Several factors complicate alloy growth, the limited bulk solubility of Sn in Ge, $x < 0.005$, a large lattice mismatch between Sn and

* Corresponding author. Tel.: +1-818-3952197; fax: +1-818-7957258.

E-mail address: haa@daedalus.caltech.edu (H.A. Atwater).

[1] Present address: Intel Corp., Mail Code RNB-2-35, 2200 Mission College Blvd., Santa Clara, CA 95052, USA.

0921-5107/01/$ - see front matter
PII: S0921-5107(01)00732-2

Ge, 14.7%, and the lower surface free energy of Sn versus Ge leading to surface segregation. Molecular beam epitaxy, a non-equilibrium growth technique, overcomes the former two difficulties yet Sn surface segregation is still problematic at typical growth temperatures, $T > 450$ °C. To overcome Sn surface segregation, low growth temperatures are necessary. Single crystal, coherent and homogeneous Sn_xGe_{1-x} epitaxial films can be grown on Ge (001) at $T < 150$ °C [4]. Ge buffer layers are grown on (001) Ge substrates at 450 °C to obtain a smooth starting surface prior to Sn_xGe_{1-x} growth. The temperature is then dropped to the appropriate growth temperature, $T = 120$–150 °C.

Reflection high energy electron diffraction (RHEED) patterns show the Sn_xGe_{1-x} epitaxial layers are single crystalline with atomically rough surfaces, consistent with post-growth characterization by high resolution X-ray diffraction and atomic force microscopy. The rms surface roughness of 500×500 nm regions Sn_xGe_{1-x} epitaxial layer increases with Sn content, 1.1 nm for $x < 0.06$ and 1.5 nm for $0.06 < x < 0.115$. Rutherford backscattering spectroscopy is used to determine the Sn composition of the Sn_xGe_{1-x} epitaxial layer. The Sn peaks are of constant height, thus, the composition is uniform and free of Sn surface segregation as seen in Fig. 1. Knowing the Sn composition, the relaxed lattice constant of Sn_xGe_{1-x} is calculated using the virtual crystal approximation which has been shown to be experimentally accurate [1]. The coherency strain parallel and perpendicular to the substrate surface are calculated as a function of the relaxed lattice constant. The angular displacement of the Sn_xGe_{1-x} (004) X-ray reflection with respect to Ge (004) was measured using X-ray rocking curve diffractometry. The (004) angular displacement yields the lattice constant in the growth direction and an experimental value for the perpendicular strain e_{zz}. In order to determine the strain in the plane of the substrate, a (422) asymmetric reflection is measured from which the in-plane strain e_{xx} is determined. The experimental values of the strain components are consistent with the strain expected in the virtual crystal approximation at the compositions measured by Rutherford backscattering spectrometry. Thus high-resolution X-ray rocking curve diffractometry of Sn_xGe_{1-x} alloys with $0.035 < x < 0.115$ and film thickness of 100 nm confirms that epitaxial layers are coherent to the Ge (001) substrate Fig. 2. Fourier transform infrared (FTIR) transmission measurements in reflectance and transmittance mode yield information regarding the dielectric function of Sn_xGe_{1-x}. Infrared reflectance is found to increase with X_{Sn}, indicating the refractive index increases with X_{Sn}, as seen in Fig. 3a. The decrease of the energy gap E_g with increasing X_{Sn} is evident in the infrared transmittance data in Fig. 3b, which indicate an absorption onset occurring at lower photon energy below 5500 cm^{-1} for higher X_{Sn}.

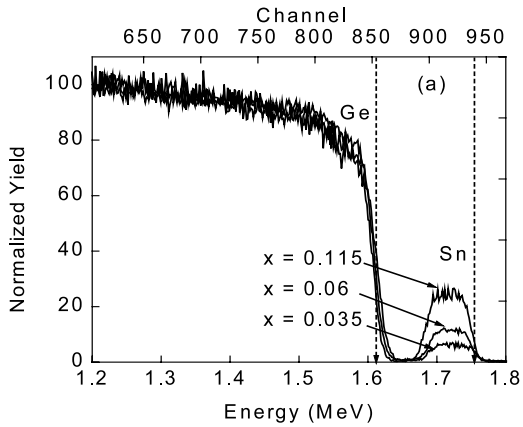

Fig. 1. Rutherford backscattering spectra with 2 MeV He^{++} for 100 nm Sn_xGe_{1-x} on Ge(001) films, sample tilted 7° to the beam direction, for $x = 0.035$, 0.06 and 0.115. Dashed lines represent the leading edge of Sn and Ge.

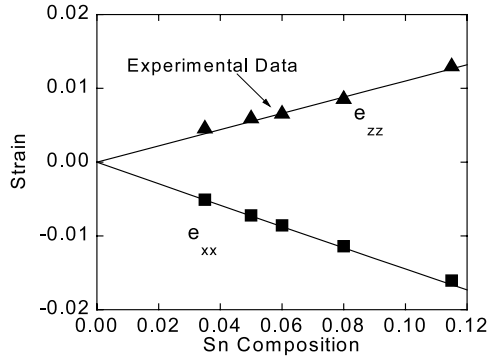

Fig. 2. Comparison between theory (solid lines) and experimental value of the in-plane, e_{xx} (squares), and perpendicular strain, e_{zz} (triangles), for 100 nm coherently-strained Sn_xGe_{1-x} films on Ge(001) with $x = 0.035$, 0.06, and 0.115.

3. Deformation potentional analysis of energy gap for strained Sn_xGe_{1-x} alloys

Deformation potential theory [5] can be used to estimate the strain-induced shifts in energy band extrema for non-polar semiconductors such as Si and Ge [6]. The effect of strain on the bandgap of Sn_xGe_{1-x} alloys is examined using a Hamiltonian derived from crystal symmetry: [7]

$$H_C = H_0^C + D_d^C(e_{xx} + e_{yy} + e_{zz}), \tag{1a}$$

$$H_V = H_0^V + D_d^V(e_{xx} + e_{yy} + e_{zz}) + 2/3\, D_u[(J_x^2 - 1/3\, J^2)e_{xx} + \text{c.p.}] + 2/3\, D'_u[1/2\,(J_y\, J_z + J_z\, J_y)\, e_{yz} + \text{c.p.}], \tag{1b}$$

where $H_0^{C,V}$ is the Hamiltonian in the absence of strain, $D_d^{C,V}$ are the conduction (valence) band deformation potential constants, J is the hole angular momentum,

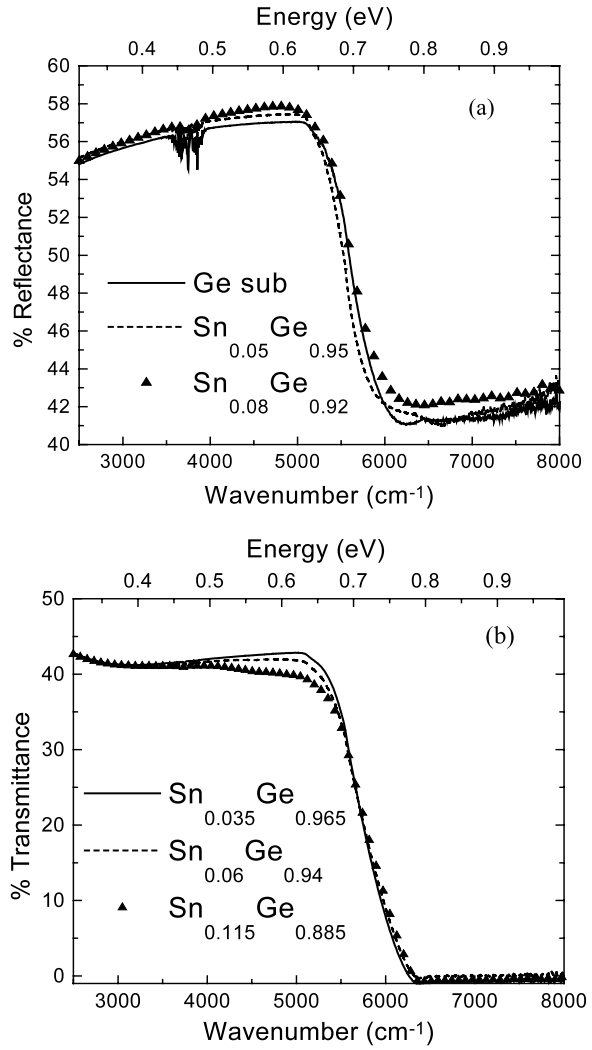

Fig. 3. FTIR spectra of 100 nm Sn_xGe_{1-x} alloys on: (a) *n*-type Ge(001) taken at 50° for $x = 0.05$ and 0.08 in reflectance mode; and (b) *p*-type Ge(001) at normal incidence for $x = 0.035$, 0.06, and 0.115 in transmittance mode.

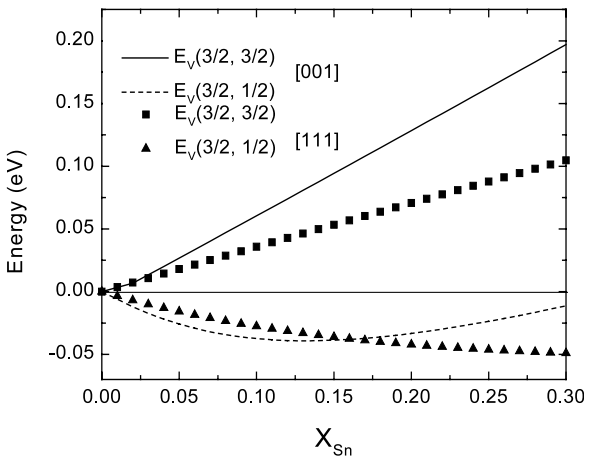

Fig. 4. Uniaxial deformation of the $E_{V,hh}$ and $E_{V,lh}$. The lines represent strain axis along [001] and the symbols [111].

and $D_u(D'_u)$ is the deformation potential constant associated with distortions along [001] ([111]). The components of the strain tensor, e_{ii}, are different for strain oriented along [001] from those with strain oriented along [111]. Due to the large lattice mismatch between Sn_xGe_{1-x} and Ge, the spin-orbit interaction must be included in the Hamiltonian to accurately characterize the energy band deformation. The strain/spin-orbit Hamiltonian is a 6×6 matrix in the (J, M_J) representation Eq. (5)[8]. As can be seen from the Hamiltonian, no mixing occurs for states with different values of M_J, thus, M_J remains a good quantum number. The energy eigenvalues Eq. (6), obtained from diagonalizing the Hamiltonian, are uniquely represented in the (J, M_J) representation.

$$H = H_e + H_{SO} =$$

$$M_J = 3/2 \quad 1/2 \quad -1/2 \quad -3/2 \quad 1/2 \quad -1/2$$

$$\begin{bmatrix} \varepsilon & 0 & 0 & 0 & 0 & 0 \\ 0 & -\varepsilon & 0 & 0 & -2\sqrt{\varepsilon} & 0 \\ 0 & 0 & -\varepsilon & 0 & 0 & -2\sqrt{\varepsilon} \\ 0 & 0 & 0 & \varepsilon & 0 & 0 \\ 0 & -2\sqrt{\varepsilon} & 0 & 0 & -\Lambda & 0 \\ 0 & 0 & -2\sqrt{\varepsilon} & 0 & 0 & -\Lambda \end{bmatrix} \tag{2}$$

$$E_V(3/2, \pm 3/2) = \varepsilon(x), \tag{3a}$$

$$E_V(3/2, \pm 1/2) = -1/2[\varepsilon(x) + \Lambda(x)] + 1/2[9\varepsilon^2(x) + \Lambda^2(x) - 2\varepsilon(x)\Lambda(x)]^{1/2}, \tag{3b}$$

$$E_V(3/2, \pm 1/2) = -1/2[\varepsilon(x) + \Lambda(x)] - 1/2[9\varepsilon^2(x) + \Lambda^2(x) - 2\varepsilon(x)\Lambda(x)]^{1/2}, \tag{3c}$$

where Λ is the spin-orbit splitting, linearly interpolated from pure Sn and Ge and

$$\varepsilon(x) = 2/3\, D_u[e_{zz}(x) - e_{xx}(x)] \quad \text{for strain axis along [001]}, \tag{4a}$$

$$\varepsilon(x) = 1/3\, D'_u \text{ for strain axis along [111]}. \tag{4b}$$

Since the deformation potential constants for pure Sn are unknown, the deformation potential constants of pure Ge are used to model strain effects on Sn_xGe_{1-x} alloy bandstructure. This is a reasonable approximation due to the low Sn content in the region of interest. The values of the deformation potential constants used in the valence band calculation are: $D_u = 3.81 \pm 0.25$ eV and $D'_u = 8.14 \pm 0.5$ eV [9]. In the presence of strain, the four-fold degeneracy of the valence band is lifted; the heavy hole valence band, $E_V(3/2, \pm 3/2)$, increases in energy while the light hole, $E_V(3/2, \pm 1/2)$, valence band decreases, as shown in Fig. 4. Thus, the valence band deformation gives rise to a decrease in E_g. $\Delta E_{V,hh}$ is larger

when the strain axis is along [001]. The conduction band energy shift for a valley in the k^i direction is given by [10]:

$$\Delta E_c^{(i)} = [\Xi_d \bar{1} + \Xi_u \{\hat{\mathbf{a}}_i\ \hat{\mathbf{a}}_i\}] * \bar{e}, \quad (5)$$

where Ξ_d, Ξ_u are the dilation and uniaxial deformation potential constants, 1 is the unit tensor, $\mathbf{a}_i$ is the unit vector in the direction of the conduction band valley, e is the strain tensor and * denotes an inner product. The mean energy shift of the conduction band extrema is [10]:

$$\Delta E_c^{(0)} = \left(\Xi_d + \frac{1}{3}\Xi_u\right)\bar{1} * \bar{e}. \quad (6)$$

Thus, the uniaxial component of the conduction band deformation is then calculated by subtracting Eq. (6) from Eq. (5). Due to the symmetry of the eight $\langle 111\rangle$ conduction band valleys around the [001] direction, the uniaxial splitting of the conduction band is zero. The symmetry is broken when the strain axis is along [111] and the uniaxial splitting is given by:

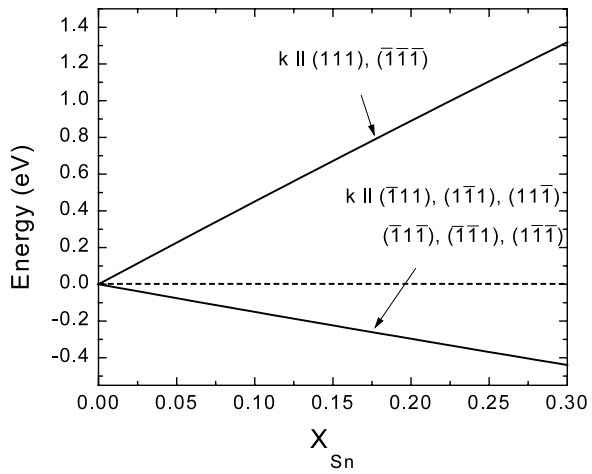

Fig. 5. Uniaxial splitting of conduction band at L_6 due to strain along [111].

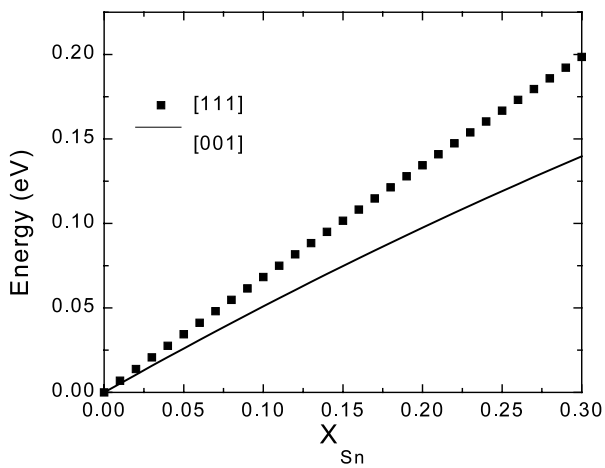

Fig. 6. Hydrostatic component of ΔE_g represented by squares for strain along [111] and a line for strain along [001].

$$\Delta E_c^{(i)} - \Delta E_c^{(0)} = 2\Xi_u e_4, \quad k^{(i)} \Rightarrow (111), (\bar{1}\bar{1}\bar{1}), \quad (7a)$$

$$\Delta E_c^{(i)} - \Delta E_c^{(0)} = -\frac{2}{3}\Xi_u e_4,$$

$$k^{(i)} \Rightarrow (\bar{1}11), (1\bar{1}1), (11\bar{1}), (\bar{1}\bar{1}1), (\bar{1}1\bar{1}), (1\bar{1}\bar{1}). \quad (7b)$$

The six conduction band valleys off the strain axis decrease in energy giving rise to a large decrease in E_g at L_6, 150 meV for $x = 0.10$, as indicated in Fig. 5. The values used for the deformation potential constants are $\Xi_u = 17.0 \pm 0.6$ and $\Xi_d = -10.88 \pm 0.47$ eV [11]. The energy band gap shift arising from dilations is expressed by:

$$\left(\Xi_d + \frac{1}{3}\Xi_u - \gamma\right)\bar{1} * \bar{e}, \quad (8)$$

where γ is the deformation potential constant associated with uniform shifts of the valence band due to dilations. Dilations, $\Delta V/V$, associated with Sn_xGe_{1-x} on Ge are negative. The sum of the three deformation potential constants in (11) is also negative, -2.9 eV; [12] thus, hydrostatic pressure increases the Sn_xGe_{1-x} bandgap, as illustrated in Fig. 6.

For epitaxial coherent Sn_xGe_{1-x} on Ge(001), the increase in $E_{V,hh}$ decreases E_g and hydrostatic component increases E_g by a comparable amount. Thus, strain does not dramatically change E_g when the stress axis is along [001], -16 meV at $x = 0.10$. Since Γ_7 and L_6 shift uniformly, the indirect to direct energy transition occurs near $x = 0.09$ as in the relaxed Sn_xGe_{1-x} alloy. Alternatively, when the strain axis is along [111], L_6 decreases due to the uniaxial component while Γ_7 increases due to the hydrostatic component. For $X_{Sn} = 0.10$, L_6 lies 150 meV below Γ_7. Hence, in the composition range of interest, $x < 0.20$, an indirect to direct energy bandgap transition does not occur for coherent Sn_xGe_{1-x} on Ge(111), as indicated in Fig. 7. Comparison between theoretical and experimental values is made in Fig. 8, which displays the experimental value of E_g determined from the onset of absorption ($\alpha = 10^3$ cm^{-1}) in FTIR transmittance measurements versus the value of E_g predicted by deformation potential theory. The agreement between the experiment and deformation potential theory is good.

4. Sn_xSi_{1-x} heterostructure growth and α-Sn quantum dot formation

In the Sn–Si system, epitaxially-stabilized metastable α-Sn_xSi_{1-x} alloys can be grown on Si (001) by temperature-modulated molecular beam epitaxy [13]. Alloy decomposition during post-growth thermal annealing of thin Sn_xSi_{1-x} alloys grown on Si (001) can initially proceed via phase separation during deposition or in a buried epitaxial layer during subsequent isothermal annealing. Confinement in a buried epitaxial layer stabilizes

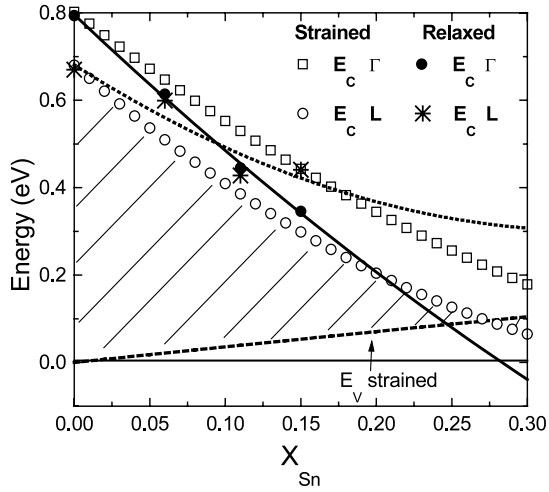

Fig. 7. Plot of E_C, Γ for strained (open squares) and relaxed (circles) [1], of E_C, L for strained (open circles) and relaxed (asterisk), and strained $E_{V,hh}$ (dash) for Sn_xGe_{1-x} on Ge(111). E_g is shaded for the strained alloy.

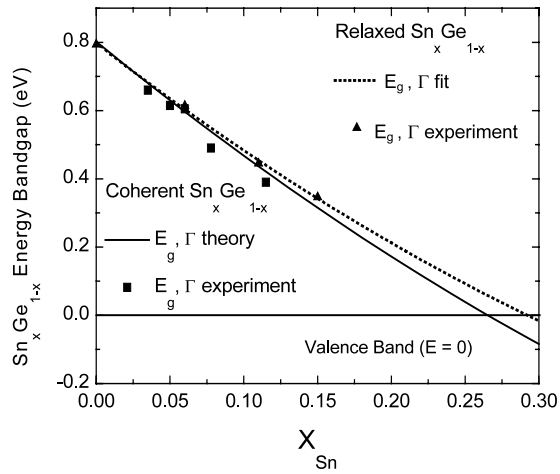

Fig. 8. Plot of E_g, Γ for strained (squares) and relaxed (triangles) [1] for Sn_xGe_{1-x} on Ge(001). The deformation potential theory is represented by a solid line.

the α-Sn cubic phase, whereas an equivalent size and density of Sn islands on the surface of (001) Si exhibits the β-Sn tetragonal phase. At the late stages of phase separation α-Sn dots grow by a coarsening mechanism with particle growth kinetics that exhibit a sub-linear power law dependence on annealing time.

Our interest in Sn quantum dots in Si is motivated by the potential for synthesis of a Si-based direct bandgap semiconductor [14]. Although quantum confinement effects are clearly observed [15,16], Ge and SiGe quantum dots are indirect band gap semiconductors. In bulk form, diamond cubic α-Sn is a direct zero band gap semiconductor, and quantum confinement is anticipated to increase the band gap at the Γ point of the Brillouin zone. As noted above, direct interband transitions have been seen in the related bulk Sn_xGe_{1-x} system [1]. Relative to growth of chemically stable alloys, growth of Sn_xSi_{1-x} is more difficult. Difficulty arises from a large lattice mismatch between α-Sn and Si (19.5%), extremely low solid solubility of Sn in crystalline Si ($\sim 5\times10^{19}$ cm^{-3}) [17], and severe Sn segregation to the surface during growth at ordinary Si epitaxy temperatures ($T > \sim 400$ °C). As a result, the usual strain-driven Stranski–Krastonow growth mode [18], which is the growth mode of Ge quantum dots on Si, cannot be achieved. These difficulties can be overcome by epitaxial growth of ultrathin alloy layers on Si at low temperatures, and subsequently annealing to form quantum dots by phase separation. All samples were grown by molecular beam epitaxy. An electron beam evaporation source and an effusion cell was used for Si and Sn deposition, respectively. Just prior to growth of the Si buffer layer, the Si (001) substrates were heated to 550 °C to obtain a clean (2 × 1) reconstructed surface. For all samples, Si buffer layers were grown at 550 °C at 0.05 nm s^{-1} to obtain a smooth Si surface prior to deposition of the Sn_xSi_{1-x} layers. After the buffer layer deposition, the growth was interrupted to cool the substrate to 170 °C prior to Sn_xSi_{1-x} alloy layer deposition. The deposited Sn_xSi_{1-x} alloy layers were 1–4 nm in thickness and 5–20% Sn in composition and the deposition rate was 4–5 ml min^{-1}. Subsequently, in order to cap the alloy layer with minimal Sn segregation to the surface, 14 nm of Si overlayer was grown at 170 °C at a growth rate of 0.03 nm s^{-1}. The details of the growth process can be found elsewhere [13]. The samples were subsequently annealed in high vacuum at temperatures ranging from 500 to 800 °C, and the structural evolution was studied using transmission electron microscopy (TEM), X-ray reflectivity rocking curve analysis and Rutherford backscattering spectrometry. Fig. 9a shows a cross sectional bright field image of an as-grown film at 170 °C with an embedded 2 nm $Sn_{0.05}Si_{0.95}$ alloy layer. The continuous dark band indicates the buried $Sn_{0.05}Si_{0.95}$ alloy layer. Fig. 9b shows the film in Fig. 9a annealed in vacuum at 800 °C for 30 min. A high resolution image of a single Sn dot is shown in Fig. 9c in which the lattice fringes between the Si matrix and the Sn dot are seen to be continuous. The precipitation of Sn-rich quantum dots is clearly observed. We note that in cross-section, TEM provides an atomic column-averaged image over the electron transparent sample of about 100 nm in thickness. Therefore, the cross-sectional image shows some overlapping dots. More insight into the morphological evolution can be obtained from plan-view electron microscopy studies. Fig. 10a–c are plan view electron micrographs of a $Sn_{0.1}Si_{0.9}$ alloy as-deposited at 170 °C, a film annealed at 500 °C for 3 h and a film annealed at 800 °C for 30 min, respectively. It should be noted that all images are bright field images taken away from strongly diffracting conditions. This was

done to reduce strain contrast in order to minimize error in the subsequent size analysis. Therefore, the resulting contrast results mainly from compositional differences. One clearly sees that the as-grown alloy layer shown in Fig. 10a has already started to phase separate into Sn-rich (dark) and Sn-deficient (light) regions. The inset shows a grey level intensity line scan through the section A-A. The intensity varies gradually in a continuous fashion as the diffuse boundary between the Sn-rich and -deficient regions is crossed. Fig. 10b shows that after the film is annealed at 500 °C for 3 h, the gradual variation in concentration has been significantly reduced, indicating further phase separation by bulk atomic transport to produce the ~ 1 nm clusters that are observed. As a result, the line scan of the intensity across B-B shows that there is a sharp drop in intensity as the cluster/matrix boundary is crossed, in addition to a gradually varying background contrast. A sharp change in composition across the boundary is a key feature of nucleation. When the film is annealed at 800 °C for 30 min, the gradual variation in contrast disappears, as is evident in Fig. 10c. As can

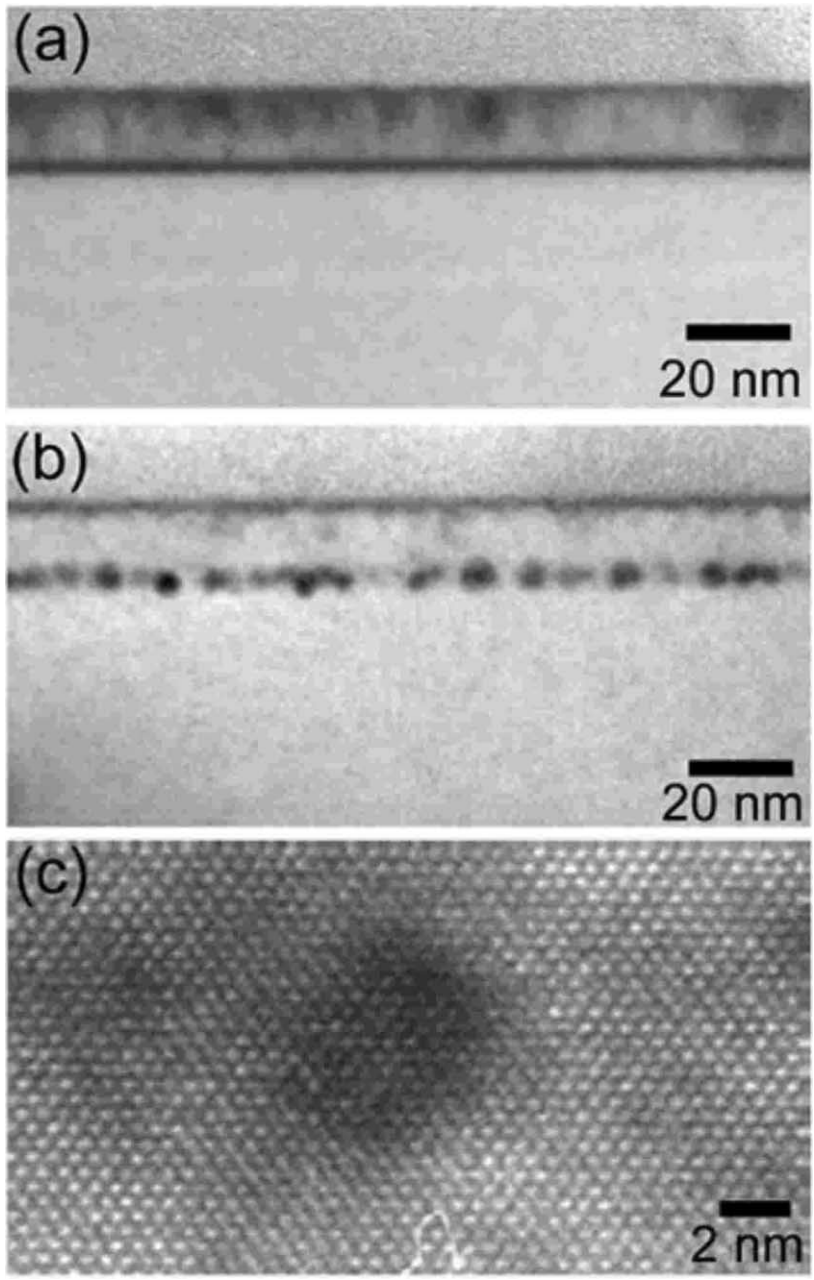

Fig. 9. ⟨110⟩ axis cross-sectional transmission electron micrographs of 2 nm $Sn_{0.05}Si_{0.95}$ capped with 14 nm Si. Bright-field images of the: (a) as-grown film at 170 °C; and (b) after annealing in vacuum at 800 °C for 30 min. In (c), high resolution image along ⟨110⟩ of one Sn dot in Si formed by decomposition of a 2 nm $Sn_{0.10}Si_{0.90}$ film capped with 14 nm Si.

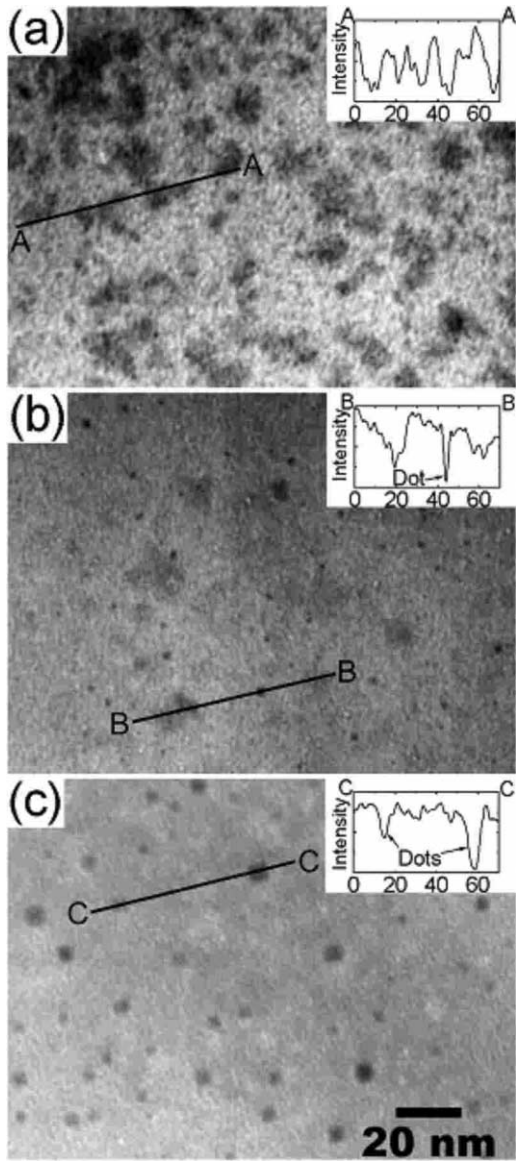

Fig. 10. Planar-view transmission electron micrographs of 2 nm $Sn_{0.10}Si_{0.90}$ capped with 14 nm Si. Bright-field transmission electron micrographs of: (a) the as-grown film at 170 °C; (b) the film annealed at 500 °C for 3 h; and (c) the film annealed at 800 °C for 30 min. The insets show intensity line-scans across A–A, B–B, and C–C, respectively. The images were taken away from strongly diffracting conditions to minimize error in dot size analysis. The contrast, therefore, comes mainly from Sn compositional differences between different regions.

be seen by the line scan C–C, there are only sharp contrast variations across the nanocrystal/matrix boundaries, and gradual variation in contrast has disappeared altogether. One also clearly sees that the average size of the nanocrystals has clearly increased. Another notable feature in Fig. 10c is that all nanocrystals appear faceted along the same crystallographic axis. The images indicate faceting along the $\langle 100 \rangle$ directions, the elastically soft directions in Si. Analysis of the integrated dot volume/area from images such as Fig. 10c, coupled with total Sn atom coverage/area measurements by Rutherford backscattering spectrometry enables an estimate of the dot composition as being pure Sn, within a composition uncertainty of approximately 15%.

Infrared absorption spectra were taken of the α-Sn quantum dots in the attenuated total reflectance geometry, in which the angle of incidence of infrared radiation reflecting from the faces of a prism-shaped crystal of high refractive index such as Si can exceed the critical angle θ_c for total internal reflection. Multiple passes can be made with a single crystal and the number of passes N scales directly with the length of the crystal l, given by $N = l/t \cot\theta$, where t is the crystal thickness and θ is the angle of incidence. The schematic geometry of the total internal reflection mode is shown in Fig. 11a. The absorption measurements were made using a Fourier transform infrared spectrometer equipped with a Ge-coated KBr beamsplitter and liquid nitrogen-cooled InSb detector. All samples were polished into trapezoids, with a bevel angle of 45°. The thickness of the samples was 450–500 μm. The tip-to-tip length l of the crystals was 25 mm, and the corresponding number of passes were $N = 50–55$ for normal incidence on the face of the beveled edge. A float zone Si (100) substrate taken from the same wafer lot as those used as substrates for the α-Sn quantum dot samples was polished into a trapezoid and used as a reference sample for background correction. The phase-separated Sn-rich Sn_xSi_{1-x} quantum dots were near the surface of the shorter face of the trapezoid, as indicated in Fig. 11a. The as-grown 2 nm $Sn_{0.10}Si_{0.90}$/Si films were polished into trapezoids and spectra were taken before and after annealing in vacuum at 800 °C for 30 min. No observable surface roughening resulted from annealing, so the absorption features are not a result of scattered radiation from roughened surfaces.

Fig. 11b indicates the absorption coefficient before and after annealing at 800 °C for 30 min. The α-Sn dot sample absorbance was normalized to the absorbance of a Si substrate of the same prism. The spectra have been translated so that the minimum value of absorbance around 2200 cm^{-1} has been taken as the baseline value of zero. Taking the optical thickness of the encapsulated alloy layer containing quantum dots to be that of the original thickness of 2 nm, and taking the number of bounces determined from the geometry enables an estimate of the absorption coefficient to be made. The spectra exhibit a broad absorption feature starting at about 0.27 eV (2250 cm^{-1}) that increases in intensity by a factor of two upon annealing. The energy of 0.27 eV does not correspond to any known intraband or interband transition with high joint density of states in bulk α-Sn, suggesting that the absorption edge is that of quantum-confined carrier absorption in an array of α-Sn quantum dots in which the variation in

dot size has inhomogeneously broadened the absorption edge. It is noteworthy that the relatively high values ($>5\times10^3$ cm^{-2}) of absorption coefficient observed are consistent with the absorption due to direct interband transitions.

After the early stage clustering via spinodal decomposition and subsequent nucleation, the late stage growth of regularly shaped nanocrystals takes place via coarsening upon annealing at elevated temperatures. For mass-conservative systems, coarsening is most readily recognized when the time evolution of growth kinetics is characterized by an increase in the average dot size and a decrease in the dot density [19]. Fig. 12a shows the isothermal evolution of dot size at a fixed temperature of 650 °C, expressed in terms of the average nanocrystal dimension $\langle r\rangle$. The parameter r is the square root of the area of the nanocrystal measured from planar view transmission electron micrographs. So $\langle r\rangle^3$ is a dimension parameter proportional to the average volume of the nanocrystals. One sees that there is a transient period where the average size increases rapidly in a short time. This transient period can be attributed to the nucleation and growth regime between the initial spinodal decomposition regime and the late-stage coarsening regime where the matrix is being depleted. Subsequently, the volume increases roughly linearly with time. The solid line is a linear fit. It is noteworthy that the growth of critical clusters follows a sublinear power law. Fig. 12b shows the size distribution after annealing at 650 °C for 2 h. The shape of the distribution does not change significantly with time. The isothermal evolution of the dot density exhibits a behavior correlated with size; after a transient period where the density drops off rapidly, the density decreases monotonically.

Late stage growth can be described by coarsening (Ostwald ripening) models when clusters larger than the average size grow at the expense of smaller ones. The driving force is the imbalance of the concentration of atoms between the equilibrium concentration of Sn at the nanocrystal/matrix interface and the Sn concentration in the matrix far removed from the nanocrystal. The cube of the critical radius increasing linearly with time is expected to occur, provided that strain does not play a significant role in mass transfer, for diffusion-limited growth of three-dimensional islands and for interface transfer-limited growth of two-dimensional islands [19]. A more complete model, however, should take into account of the effect of strain. The two late-stage trends, namely increasing average nanocrystal size and decreasing nanocrystal density with time, indicate that the dot grows by a coarsening mechanism.

The presence of facets along the elastically soft $\langle100\rangle$ directions, as seen in Fig. 10, is not unexpected, in light of the presence of a large misfit strain, since the interfacial stress can be most efficiently relieved along such directions. In planar view, many nanocrystals look almost square-shaped. In the corresponding cross-sectional image along the [110] direction in Fig. 9, however, the nanocrystals almost look spherical, and the presence of facets is not obvious. This is not inconsistent with what one would observe, however, if the shape of the nanocrystals is similar to that of the equilibrium shape of Si, which has been demonstrated to be a tetrakaidecahedron from the equilibrium shape of voids in Si [20]. The equilibrium shape of Si is composed mainly of {111} and {100} facets. Along $\langle110\rangle$ axis cross section, the nanocrystal then would resemble an octagon, and along $\langle100\rangle$ planar view the

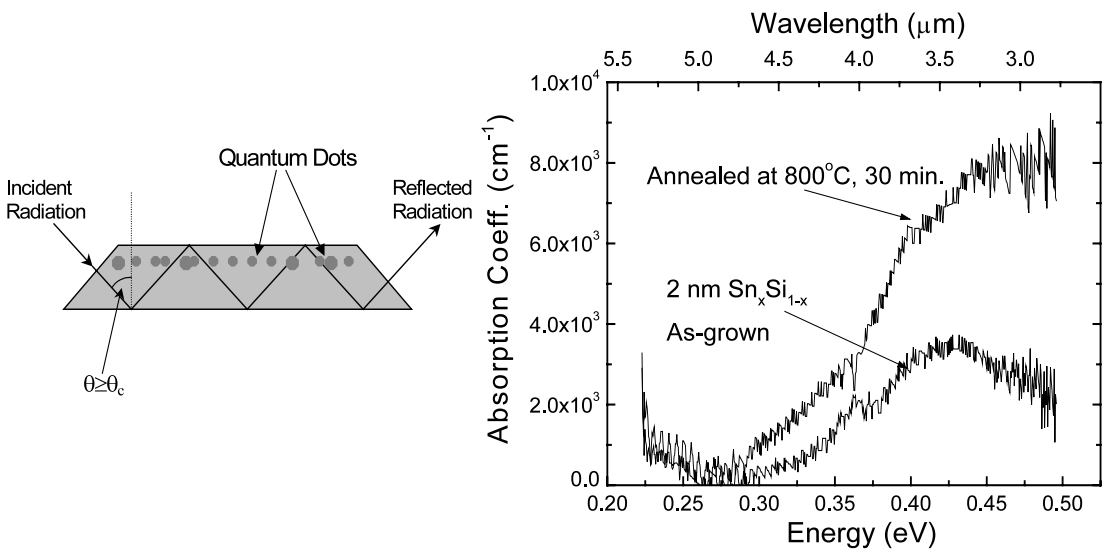

Fig. 11. Multiple internal reflectance Fourier transform infrared spectroscopy (MIR-FTIR) measurements of absorption coefficient of 2 nm $Sn_{0.10}Si_{0.90}$ capped with 14 nm Si. Shown are schematic of sample configuration at left and at right, data for as-grown film at 170 °C and film annealed at 800 °C for 30 min.

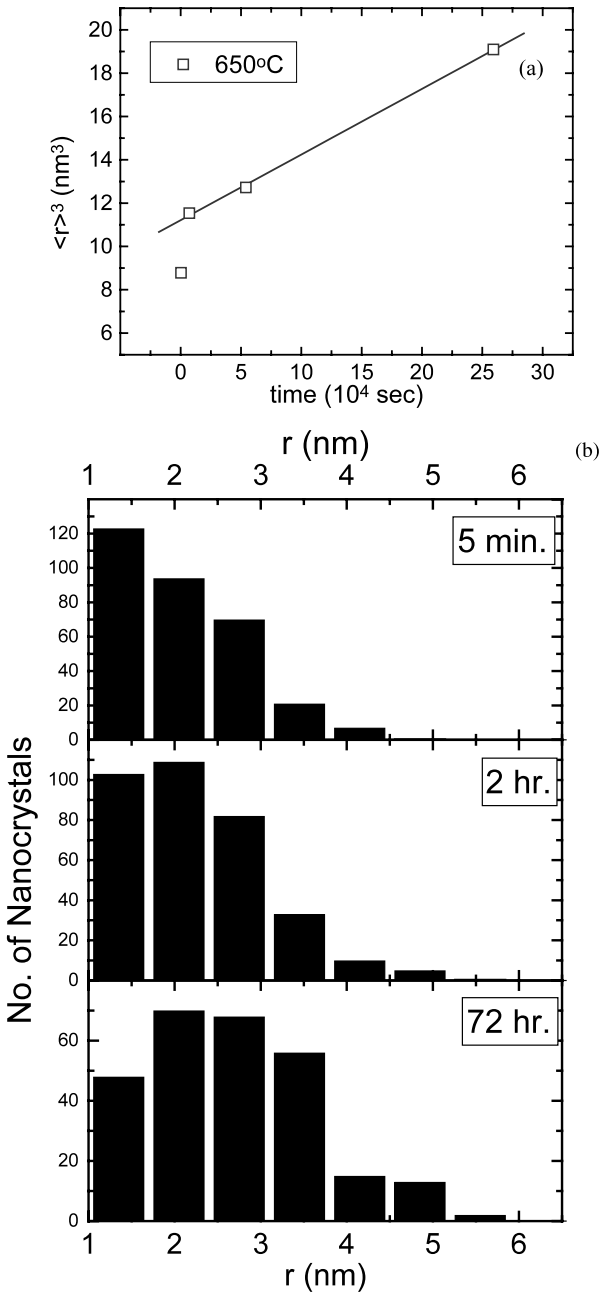

Fig. 12. Coarsening kinetics for α-Sn dots during thermal annealing at $T = 650$ °C. In (a), variation of dot volume with time; and (b) dot size distributions derived from plan-view transmission electron microscopy.

nanocrystal would resemble a square. If some facets are slightly rounded, as observed in [20], the observed shape of Sn_xSi_{1-x} nanocrystals would be consistent with the equilibrium shape of Si.

5. Conclusions

Sn_xGe_{1-x} alloys are a unique example of band-structure engineering of a direct gap group IV semiconductor alloy. Deformation potential models have been used to determine the effect of strain on E_g for two cases: Sn_xGe_{1-x} on Ge(111) and Sn_xGe_{1-x} on Ge(001). The model predicts a large uniaxial splitting at L_6 and the absence of an indirect to direct energy bandgap transition in the composition range of interest, $x < 0.30$, for Sn_xGe_{1-x} alloys on Ge(111) substrates. Experimental results of E_g for strain-relieved and pseudomorphically strained Sn_xGe_{1-x} on Ge(001) are consistent with the small decrease in E_g with strain that is predicted by deformation potential theory.

We have also observed formation of coherently strained Sn_xSi_{1-x} quantum dots inside Si matrix by two-dimensional phase separation from an epitaxally stabilized Sn_xSi_{1-x} metastable solid solution. Transmission electron microscopy studies reveal that the phase separation initially proceeds by spinodal decomposition and subsequent thermal annealing results in the nucleation of regularly shaped Sn-rich Sn_xSi_{1-x} quantum dots. The nucleated dots grow by a coarsening mechanism. Cross-sectional high-resolution transmission electron microscopy reveals that the dots are completely coherent with the Si matrix and that the shape of the nanocrystals resembles that of the equilibrium shape of Si, namely tetrakaidecahedron dominated by {100} and {111} facets.

Acknowledgements

Support from the National Science Foundation is gratefully acknowledged.

References

[1] G. He, H.A. Atwater, Phys. Rev. Lett. 79 (1997) 1937.
[2] D.W. Jenkins, J.D. Dow, Phys. Rev. B 36 (1987) 7994.
[3] W. Wegscheider, et al., J. Cryst. Growth 123 (1992) 75.
[4] R. Ragan, H.A. Atwater, Appl. Phys. Lett. 77 (2000) 3418.
[5] J. Bardeen, W. Shockley, Phys. Rev. 80 (1950) 72.
[6] R. People, Phys. Rev. 32 (1985) 1405.
[7] W.H. Kleiner, L.M. Roth, Phys. Rev. Lett. 2 (1959) 334.
[8] H. Hasegawa, Phys. Rev. 129 (1963) 1029.
[9] F.H. Pollak, M. Cardona, Phys. Rev. 172 (1968) 816.
[10] C. Herring, E. Voigt, Phys. Rev. 101 (1956) 944.
[11] N.L. Kang, J.Y. Ryu, S.D. Choi, J. Phys. Soc. Jpn. 67 (1998) 2439.
[12] G.E. Pikus, G.L. Bir, Fiz. Tverd. Tela 1 (1959) 1642 [Sov. Phys. Solid State 1 (1960) 1502].
[13] K.S. Min, Harry A. Atwater, Appl. Phys. Lett. 72 (1998) 1884.
[14] R.A. Soref, C.H. Perry, J. Appl. Phys. 69 (1991) 539.
[15] R. Apetz, L. Vescan, A. Hartmann, C. Dieker, H. Luth, Appl. Phys. Lett. 66 (1995) 445.

[16] H. Sunamura, N. Usami, Y. Shiraki, S. Fukatsu, Appl. Phys. Lett. 66 (1995) 3024.
[17] R. Swalin, Thermodynamics of Solids, 2nd, John Wiley and Sons, New York, 1972, p. 141.
[18] M. Krishnamurty, J.S. Drucker, J.A. Venables, J. Appl. Phys. 69 (1991) 6461.
[19] M. Zinke-Allmang, L.C. Feldman, M.H. Grabow, Sur. Sci. Rep. 16 (1992) 377.
[20] D.J. Eaglesham, A.E. White, L.C. Feldman, N. Moriya, D.C. Jacobson, Phys. Rev. Lett. 70 (1993) 1643.